

11-1-2022

Quantitative tumor depth determination using dual wavelength excitation fluorescence

Christine M. O'Brien
Washington University School of Medicine in St. Louis

Kevin W. Bishop
Washington University School of Medicine in St. Louis

Haini Zhang
Washington University School of Medicine in St. Louis

Xiao Xu
Washington University School of Medicine in St. Louis

Leo Shmuylovich
Washington University School of Medicine in St. Louis

See next page for additional authors

Follow this and additional works at: https://digitalcommons.wustl.edu/oa_4



Part of the [Medicine and Health Sciences Commons](#)

Please let us know how this document benefits you.

Recommended Citation

O'Brien, Christine M.; Bishop, Kevin W.; Zhang, Haini; Xu, Xiao; Shmuylovich, Leo; Conley, Elizabeth; Nwosu, Karen; Duncan, Kathleen; Mondal, Suman B.; and Sudlow, Gail, "Quantitative tumor depth determination using dual wavelength excitation fluorescence." *Biomedical Optical Express*. 13, 11. 5628 - 5642. (2022). https://digitalcommons.wustl.edu/oa_4/1091



This Open Access Publication is brought to you for free and open access by the Open Access Publications at Digital Commons@Becker. It has been accepted for inclusion in 2020-Current year OA Pubs by an authorized administrator of Digital Commons@Becker. For more information, please contact vanam@wustl.edu.

Authors

Christine M. O'Brien, Kevin W. Bishop, Haini Zhang, Xiao Xu, Leo Shmuylovich, Elizabeth Conley, Karen Nwosu, Kathleen Duncan, Suman B. Mondal, and Gail Sudlow



Quantitative tumor depth determination using dual wavelength excitation fluorescence

CHRISTINE M. O'BRIEN,^{1,2,6,7} KEVIN W. BISHOP,¹  HAINI ZHANG,^{1,2} XIAO XU,¹ LEO SHMUYLOVICH,^{1,3} ELIZABETH CONLEY,¹ KAREN NWOSU,¹ KATHLEEN DUNCAN,¹ SUMAN B. MONDAL,¹  GAIL SUDLOW,¹ AND SAMUEL ACHILEFU^{1,2,4,5,6,8}

¹Department of Radiology, Washington University School of Medicine, 4515 McKinley Ave., St. Louis, MO, 63110, USA

²Department of Biomedical Engineering, Washington University in St. Louis, 1 Brookings Drive St. Louis, MO 63130, USA

³Division of Dermatology, Department of Medicine, Washington University School of Medicine, 4960 Children's Place, St. Louis, MO 63110, USA

⁴Department of Medicine, Washington University School of Medicine, 4960 Children's Place, St. Louis, MO 63110, USA

⁵Department of Biochemistry and Molecular Biophysics, Washington University School of Medicine, 660 S. Euclid Ave., St. Louis, MO 63110, USA

⁶These authors contributed equally to this work

⁷c.obrien@wustl.edu

⁸Samuel.Achilefu@UTSouthwestern.edu

Abstract: Quantifying solid tumor margins with fluorescence-guided surgery approaches is a challenge, particularly when using near infrared (NIR) wavelengths due to increased penetration depths. An NIR dual wavelength excitation fluorescence (DWEF) approach was developed that capitalizes on the wavelength-dependent attenuation of light in tissue to determine fluorophore depth. A portable dual wavelength excitation fluorescence imaging system was built and tested in parallel with an NIR tumor-targeting fluorophore in tissue mimicking phantoms, chicken tissue, and in vivo mouse models of breast cancer. The system showed high accuracy in all experiments. The low cost and simplicity of this approach make it ideal for clinical use.

© 2022 Optica Publishing Group under the terms of the [Optica Open Access Publishing Agreement](#)

1. Introduction

Real-time intraoperative imaging is revolutionizing surgical oncology practice worldwide by providing continuous views of delicate anatomy and tumor boundaries throughout surgery, during which the tissue in and around the surgical cavity is significantly deformed. Intraoperative imaging techniques rely on either intrinsic contrast or contrast agents, many of which are tumor-targeted [1]. These approaches aid in minimizing harm from accidental injury of nerves or large blood vessels, and help demarcate cancerous tissue for complete resection while preserving nearby healthy tissue. There are a number of excellent review articles [1–4] highlighting various image-guided surgery techniques spanning ultrasound, nuclear, optical, and hybrid approaches, all of which have unique strengths and limitations. Strengths of optical approaches, and in particular fluorescence-guided surgery (FGS), include the ability to achieve real-time, contact-free, high-contrast images with less expensive and compact hardware. These characteristics allow the expansion of FGS to rural and underserved communities, beyond the cutting-edge medical centers where most image-guided surgery technologies are currently used.

To reach its full potential in cancer surgery, FGS must move beyond localizing tumor tissue and sparing healthy tissue. Clinical investigations have found superior outcomes in solid tumor resection are achieved when the tumors are removed with a healthy margin of tissue completely

surrounding the tumor (negative margin) [5,6]. The optimum clear margin thickness varies by tumor type and is an active area of research and debate for certain cancers [7–9].

Several strategies exist for assessing margin extent. Histopathology serves as the gold standard for determining whether negative margins were achieved. However, pathological analysis is typically done post operatively (days after surgery), meaning any residual tumor cannot be further resected without a second surgery. Existing intraoperative approaches to assess margin extent include specimen radiography, which is fast but has shown poor accuracy [10], and frozen section analysis, which has high accuracy but is labor/infrastructure intensive and can require surgeons to wait up to 50 minutes while the patient is in the operating room [11], extending surgery time. FGS is a promising alternative to these techniques, enabling accurate, real-time assessment of surgical margins in the operating room. This would allow surgeons to iteratively resect a tumor until negative margins are achieved, potentially shortening surgery time and reducing the likelihood that a second surgery will be required.

A key challenge in applying FGS to margin assessment is that the selected imaging technique must be able to quantitatively measure the depth of cancer cells several millimeters beneath the surface of an intact excised specimen (Fig. 1). FGS approaches often take advantage of near-infrared (NIR) fluorescent dyes, which can be detected 1–2 cm below the tissue surface [12]. Numerous strategies have been employed to address this critical need in FGS, including fluorescence tomography [13–16], fluorescence lifetime topography [17], fluorescence light-sheet microscopy [18,19], fluorescence laminar optical tomography [20], and ratiometric fluorescence imaging from multi-wavelength excitation [21–25]. The arguably least expensive and simplest technique, both conceptually and technically, is ratiometric fluorescence imaging, which takes advantage of the wavelength-dependent attenuation of light in tissue to provide depth information independent of fluorophore concentration. This method uses minimal hardware and basic data processing, and thus has high potential for successful translation to oncologic surgery across a

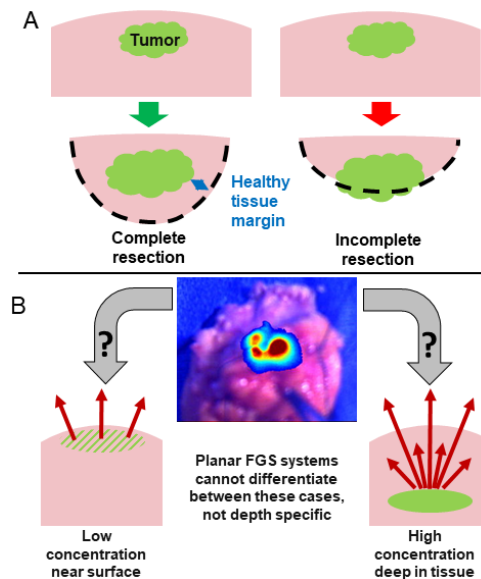


Fig. 1. (A) A margin of healthy tissue completely surrounding excised solid tumors is required for complete resection. (B) Fluorescence guided surgery (FGS) can aid in achieving full margins but currently cannot determine tumor depth from the surface. Since NIR probes can be detected beyond a centimeter deep, determining their axial location is important to ensure full margins are achieved without unnecessary sacrifice of healthy tissue.

range of economies and settings. Ratiometric fluorescence imaging has been recently used in FGS to determine the depth of brain tumors from the exposed brain surface based on selective accumulation of a visible fluorophore called protoporphyrin IX in tumors following administration of 5-aminolevulinic acid [22].

This ratiometric fluorescence depth mapping approach has not yet been used with NIR fluorescence agents, which have increased contrast and penetration depth compared with tissue autofluorescence or exogenous visible-spectrum agents [26]. Because of these advantages, targeted NIR agents are being developed in abundance for FGS applications [1,27,28]. Herein, we report a ratiometric fluorescence imaging strategy using tumor-targeted NIR fluorophore, LS301, that selectively binds to phosphorylated annexin A2, which is overexpressed in tumors [29]. Critical advantages of this NIR depth profiling approach include simple instrumentation, rapid image processing and analysis, and improved tissue penetration and tumor contrast, making it well-suited for clinical translation and integration in FGS.

2. Materials and methods

2.1. Tumor targeting contrast agent LS301

LS301 is an octapeptide labeled with an NIR fluorophore that selectively binds to phosphorylated Annexin A2, a protein that is over expressed in multiple types of solid tumors [29]. The fluorophore has a broad excitation spectrum, spanning ~650-810 nm, which was measured using a spectrofluorimeter (Fluorolog, Horiba, New Jersey, USA). LS301 has a similar fluorescence excitation and emission profile as ICG, it has demonstrated safety in animal studies [29], and clinical trials in breast cancer patients are underway (ClinicalTrials.gov Identifier: NCT02807597).

2.2. Fluorophore depth determination from dual wavelength excitation

Light intensity attenuates at different rates across the visible and near-infrared spectrum due to wavelength-specific characteristics of optical absorbers and scatterers in tissue [30]. Upon illumination of a fluorophore with two different excitation wavelengths, the intensity falloff with depth at each wavelength is based on the optical properties of the tissue which govern the slope, such that the natural log of the ratio of the fluorescence intensity (which is mathematically equivalent to the differences of the natural logs) generated by each wavelength has a linear relationship to the depth of the fluorophore [21,23,31] (Fig. 2):

$$\ln\left(\frac{I_{\lambda 1}}{I_{\lambda 2}}\right) = \ln(I_{\lambda 1}) - \ln(I_{\lambda 2}) = \ln(\Gamma) = m * d + b \quad (1)$$

Importantly, the ratio is also independent of concentration [21,23,31]. Reports have demonstrated that the slope (m) of the line governing the relationship between depth and fluorescence ratio can be estimated [23] using optical properties μ_a and μ_s' if they are known or can be measured:

$$m = \frac{1}{\delta^{\lambda 1}} - \frac{1}{\delta^{\lambda 2}} \quad (2)$$

where

$$\delta = \sqrt{\frac{D}{\mu_a}} \quad (3)$$

and

$$D = \frac{1}{3(\mu_a + \mu_s')} \quad (4)$$

The y-intercept (b) can be solved based on knowledge of how light will diffuse in the medium at each wavelength which is described by the optical diffusion coefficient D . Taking the ratio of

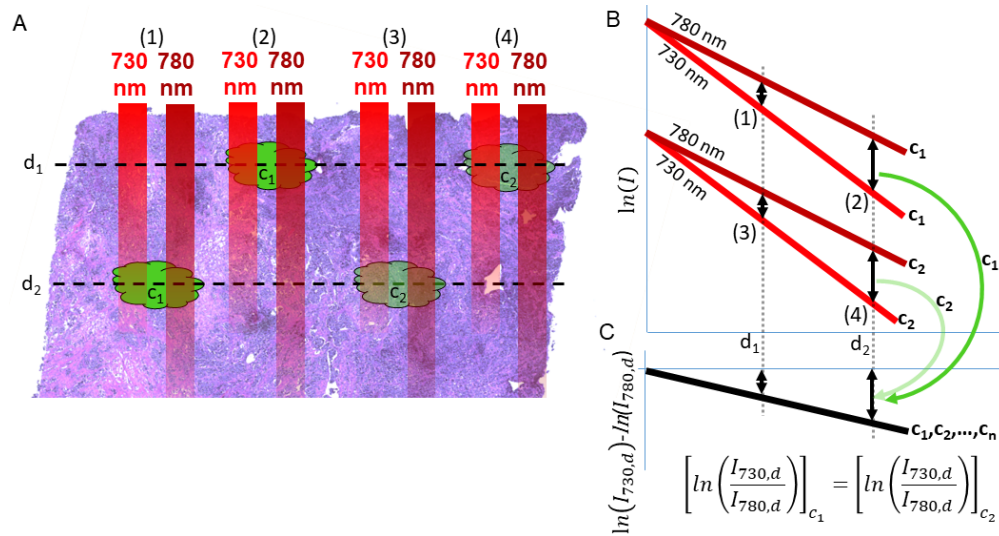


Fig. 2. Dual wavelength excitation for fluorophore depth determination. A) Schematic of wavelength-dependent attenuation of light and interaction with fluorophores of different concentrations (c_1 – dark green, c_2 – light green). B) If the log of the fluorescence generated at two excitation wavelengths, 730 and 780 nm, is plotted against depth for two different concentrations of fluorophore, four different intensities result for a single depth. C) However, if the log of the fluorescence ratio generated by 730 and 780 nm excitation is plotted, a unique solution is found for each depth, regardless of concentration. (Abbreviations: d – depth, c – concentration, I – fluorescent intensity) Green arrows correspond to the concentration of fluorophore (dark green – c_1 , light green – c_2). Identical black arrows shown at d_1 and d_2 demonstrate that the difference in fluorescent intensity generated by each excitation wavelength equals the log of their ratio, regardless of fluorophore concentration.

the diffusion coefficients provides the baseline relative fluorescence ratio expected as a function of the tissue's optical properties:

$$b = \ln\left(\frac{D^{\lambda_2}}{D^{\lambda_1}}\right) \quad (5)$$

In the current work, published and measured optical properties are used with Eq. (2)-(5) to calculate fluorophore depth in NIR dual wavelength excitation experiments.

2.3. Portable dual wavelength excitation fluorescence system

A fluorescence imaging system was constructed using 730 and 780 nm LEDs (M730L5 and M780L3, Thorlabs, Newton, NJ, USA) and a monochrome CMOS camera (STC-MBS500U3V, SenTech, Willow Grove, PA, USA). The 730 and 780 LED illumination was aligned using a cage cube and dichroic filter (#87-062, 757nm, 25.2 × 35.6mm, Edmund Optics, Barrington, NJ, USA). A high-pass filter (EdgeBasic Long Wave Pass 785, Semrock, Rochester, NY, USA) was placed in front of the camera to detect fluorescent light and reject excitation light. The LEDs were controlled using an LED driver that allowed modulation of each LED (DC4104, Thorlabs, Newton, NJ, USA). In addition, an 850 nm LED (M850L3, Thorlabs, Newton, NJ, USA) was used to create a brightfield image such that fluorescent images could be correlated with the real-world view of the sample being interrogated. Modulation was achieved by connecting the LED driver external modulation cable to an electrical relay (4 Channel DC 5V Relay Module, JBtek, Surrey, BC, Canada) that was interfaced with an Arduino Uno board (Arduino, Somerville, MA, USA) which was controlled by a custom graphical user interface (GUI) developed using Matlab's App

Designer. The camera was also controlled using the Matlab GUI and acquired sequential 730 nm excitation fluorescence, 780 nm excitation fluorescence, and 850 nm brightfield images of each sample of interest.

2.4. Ratiometric fluorescence imaging analysis

The GUI also performs rapid image analysis by first capturing a fluorescent image at 730 and 780 nm excitation wavelengths of a custom wide-field uniform NIR fluorescence reference to account for spatial differences across the LED illumination profiles. The wide-field phantom images are each segmented using a threshold $t \geq R_{\lambda\max} / 2$, where $R_{\lambda\max}$ is the maximum reference image intensity acquired with LED_{λ} . Only pixels in which both LEDs met the threshold are included for subsequent analysis and this defines the imaging region of the 730 and 780 nm LEDs. After segmentation, a wide-field correction ($C_{\lambda}(x,y)$) is calculated for each fluorescence reference using equation:

$$C_{\lambda}(x,y) = \frac{R_{\lambda\max}}{R_{\lambda}(x,y)} \quad (6)$$

where $R_{\lambda}(x,y)$ is the raw reference image acquired with LED_{λ} . The correction is then applied to all subsequent fluorescence images. Following wide-field correction, pairs of 730 and 780 fluorescence images are analyzed by taking the natural log of the ratio of their wide-field corrected images:

$$\ln(\Gamma(x,y)) = \ln\left(\frac{I_{\lambda 1}(x,y) * C_{\lambda 1}(x,y) * P_{\lambda 2\max} * A_{\lambda 2}}{I_{\lambda 2}(x,y) * C_{\lambda 2}(x,y) * P_{\lambda 1\max} * A_{\lambda 1}}\right) \quad (7)$$

where I_{λ} is the fluorescent image taken using excitation λ , $P_{\lambda\max}$ is the maximum power measured in the imaging plane using an optical power meter, and A_{λ} is the fluorophore absorbance at λ . As described by Kolste et al. [23], there is a linear relationship between the natural log of the fluorescence ratio and fluorophore depth (d) as shown in Eq. (1). If the optical properties are known, the y-intercept can be solved using Eq. (5). Alternatively, the y-intercept can be ignored by normalizing all measurements to measurements made when the fluorophore is known to be at the surface (depth = 0), such as the tumor surface in fluorescence-guided surgery:

$$\ln\left(\frac{\Gamma(x,y)}{\Gamma(x,y)_{@d=0}}\right) = m * d \quad (8)$$

As described above, the optical properties of the tissue can be used to calculate the slope m , and depth d , can be solved:

$$d = \frac{\ln\left(\frac{\Gamma(x,y)}{\Gamma(x,y)_{@d=0}}\right)}{m} \quad (9)$$

2.5. Optical property determination

Optical properties were measured using diffuse reflectance spectroscopy (DRS) with a single source and detector pair, and validated using an integrating sphere (IS). Diffuse reflectance spectroscopy was performed using a one-to-four fan out fiber bundle (BFL44LS01, Thorlabs, Newton, NJ). The two outer fibers at the common end were used for measurements, with their opposite ends connected to a halogen lamp (HL-2000-HP, Ocean Insight, Orlando, FL, USA) or a spectrometer (Flame spectrometer, Ocean Optics, Orlando, FL, USA). Reference measurements were taken using a large Spectralon standard that is 99% reflective at the wavelengths measured. A custom optical fiber holder was 3D printed to take diffuse reflectance images perpendicular from the Spectralon standard at a 2 mm distance. The maximum integration time that could be used without spectrometer saturation during lamp illumination was used to capture the reference spectrum (R_{ref}) and all subsequent background and sample spectra. A background measurement ($R_{\text{ref_bg}}$) was taken of the reference measurement setup using all of the same conditions except

the halogen lamp was turned off. Samples were measured by placing the common end of the fiber optic probe in gentle perpendicular contact with the sample and taking measurements with the halogen lamp on (R_s) and off (R_{s_bg}). Diffuse reflectance measurements (R_d) were processed as follows:

$$R_d(\lambda) = \frac{R_s(\lambda) - R_{s_bg}(\lambda)}{R_{ref}(\lambda) - R_{ref_bg}(\lambda)} \quad (10)$$

Optical properties were extracted by solving for R_d at a known source-detector distance under conditions of spectral constraint (Eq. (18) from Ref. [32] and Eq. (8.17) from Ref. [33]), in which the spectral shapes of tissue chromophores and scattering were used to create a forward R_d model at the same radial distance as the experiment. The R_d equation at a fixed source-detector distance includes absorption coefficient, reduced scattering coefficient, ratio of the refractive index of tissue to the refractive index of air, and the source-detector distance [32,33]. The optical absorption coefficient was treated as a linear combination of individual chromophores as described by Jacques [30]:

$$\mu_a = c_1 * \mu_{a1}(\lambda) + c_2 * \mu_{a2}(\lambda) + \dots c_n * \mu_{an}(\lambda) \quad (11)$$

Where C_1 through C_n are weighting coefficients used instead of total concentration and path length because these are difficult to measure in tissue. In cases where μ_a of a particular chromophore is well characterized in tissue, the weighting coefficient C can be considered a volume fraction of the chromophore in the sample [30]. The chromophore spectra that were included in the spectral fitting were based on the chromophores expected to be found in the tissue or synthetic phantom material in the wavelength range measured (nigrosin for the synthetic phantom, oxy- and deoxyhemoglobin for the chicken tissue, and beta carotene, oxy- and deoxyhemoglobin for the in vivo mouse tissue). The reduced scattering coefficient was modeled as a power function with two fit parameters, a and b :

$$\mu_s(\lambda) = a * \left(\frac{\lambda}{500(nm)}\right)^{-b} \quad (12)$$

where a is the reduced scattering coefficient at 500 nm, which scales the spectrum from Ref. [32] and b represents the scattering power, which governs the rate of change of scattering with increasing wavelength [30]. A spectral fitting routine shared publicly by Jacques [34] was modified by substituting the total R_d equation from Farrell et al. (Equation (22) from Ref. [32]) to the R_d equation at a set source-detector difference (Eq. (18) from Ref. [32] and Eq. (8.17) from Ref. [33]). The least-squares fitting routine was used to minimize the difference between the measured R_d spectrum and the diffusion model prediction, and output absorption weight coefficients and the reduced scattering coefficient a and b parameters that minimized the difference between the two spectra. These values were used to construct sample $\mu_a(\lambda)$ and $\mu_s(\lambda)$ spectra that were used for calculating the slope and y-intercept of the dual wavelength excitation fluorescence imaging system.

Integrating sphere measurements were conducted following the single integrating sphere measurement protocol in the Inverse Adding-Doubling manual [35]. Reflectance and transmittance values were calculated according to the manual and input into Inverse Adding-Doubling code for extraction of wavelength-dependent optical absorption and optical scattering properties [35]. The TiO_2 scattering anisotropy was set at 0.6 [36], and chicken breast tissue scattering anisotropy was set at 0.9 [37]. Measurements were acquired using a Newport integrating sphere (819C-IS-5.3, Newport Corporation, Irvine, CA, USA), a spectrometer (Flame spectrometer, Ocean Optics, Orlando, FL, USA), and broad band light was provided using a halogen lamp (HL-2000-HP, Ocean Insight, Orlando, FL, USA).

2.6. Synthetic optical tissue mimicking phantom fabrication

For wide-field correction, a large (13 cm diameter) NIR fluorescence reference standard was created by mixing polyurethane (WC-783 A/B, BJB Enterprises, Tustin, CA) with titanium dioxide (TiO₂) (titanium (IV) oxide anatase, Product no. 637254-50G, Sigma Aldrich, St. Louis, MO) as a scattering agent and IR125 (IR-125, 09030, Exciton Inc., Lockburne, OH) as an NIR fluorophore [38], which has similar absorption and emission spectra to LS301 [29]. The phantom base was made by first mixing 100 mL of polyurethane part A with 150 mg of TiO₂ and 198 μ L of IR125 stock solution (1 mM in DMSO). The mixture was sonicated for 20 minutes while stirring to disaggregate the TiO₂. Next, 90 mL of polyurethane part B was added and mixed for an additional 5 minutes. The mixture was then poured into a custom 3D printed shallow well (made from polylactic acid (PLA) filament) with inner dimensions of 13 cm diameter and 1.5 cm height and allowed to set in a light-tight container for 48 hours.

Thin tissue-mimicking phantom discs of varying thicknesses were created using a polyurethane base [39] that was poured into a PDMS mold, which allowed the polyurethane discs to be easily removed. To make the PDMS mold, first a custom 3D printed mold box (PLA) was made with raised pillars of varying heights ranging from 1–5 mm which subsequently served as wells for the polyurethane discs. After printing, the 3D printed mold cast was silanized to allow for easier removal of PDMS from the cast. The 3D printed mold cast was placed in a desiccator with a conical tube that had 10 μ L of trichlorosilane (CAS #: 78560-45-9, Gelest, Morrisville, PA, USA). The desiccator was then sealed and vacuum was applied for 20 minutes, followed by turning the vacuum off and waiting an additional 20 minutes, resulting in a silanized 3D printed mold cast. The PDMS mold was made by mixing 100 mL of silicone elastomer base with 10 mL of curing agent (Sylgard 184 Silicone Encapsulant Clear 3.9 Kg Kit, Dow, Midland, MI, USA) manually for 5 minutes and then poured into the 3D printed mold cast where it was left to cure overnight. The polyurethane tissue-mimicking phantom was made by combining 75 mL of polyurethane part A with 138.26 mg of TiO₂ for optical scattering and 22.35 mg of nigrosin powder for optical absorption (Product No. 198285-25G, Sigma Aldrich, St. Louis, MO, USA) in a sonicator for 20 minutes while manually mixing. The mixture was then combined with 67.5 mL of polyurethane part B and manually mixed for an additional 5 minutes. The polyurethane mixture was then carefully poured into the PDMS mold to create discs of varying thicknesses and cured for 48 hours.

A NIR fluorophore phantom was made similarly to the tissue-mimicking phantom discs, using a 3D printed mold cast and PDMS mold as described above to make 1 cm diameter polyurethane phantoms. The polyurethane phantom was made by combining 25 mL of polyurethane part A with 48 mg of TiO₂ and 48 μ L of IR125 stock solution (1 mM IR125 in DMSO) and mixing in a sonicator for 20 minutes. The mixture was combined with 22.5 mL of polyurethane part B and stirred for 5 minutes. The mixture was then poured into the PDMS mold and left to sit for 48 hours in a light tight container, yielding a 1 μ M IR125 tissue-mimicking polyurethane phantom.

2.7. Chicken tissue phantom

To minimize tissue deformity and enable integrating sphere measurements of chicken breast tissues, custom ring-based tissue holders were built. Rings (3 cm outer diameter, 2.6 cm inner diameter) of varying heights were 3D printed and Saran wrap was glued to their bottoms to hold the tissue in place. Chicken breast tissue was obtained from the grocery store and frozen. The frozen tissue was placed on a mandoline and sliced to thicknesses ranging from 0.5–5 mm. Frozen slices were placed into the 3D printed rings with corresponding heights and trimmed to fit within the rings. The top of the rings were then sealed with Saran wrap and superglue to make a liquid-tight tissue holder. The thickness of the tissue inside the rings was measured using calipers. The tissue rings were kept on ice until ready for measurement, in which case they were thawed for 10 minutes prior to imaging on top of a 96 well plate filled with LS301 NIR fluorophore.

2.8. Validation in phantoms and tissue

The ability of the dual wavelength fluorescence and diffuse reflectance spectroscopy system to determine fluorophore depth was first validated by layering synthetic tissue-mimicking phantoms of increasing thickness above an NIR fluorophore phantom and predicting the depth of the fluorophore beneath the synthetic tissue layers. The tissue-mimicking phantoms were measured with calipers three times and the average result was considered the true thickness for each sample. The NIR fluorophore phantom was first imaged alone using the dual wavelength fluorescence imaging system as described above, followed by imaging with synthetic tissue-mimicking phantom discs of increasing thickness placed above the NIR fluorophore phantom. This was repeated for four thicknesses of synthetic tissue-mimicking phantom. Diffuse reflectance spectroscopy was performed on the synthetic tissue-mimicking phantom, as well as an integrating sphere measurement of one of the phantom discs for optical property validation. The ratiometric fluorescence images were normalized to the zero thickness tissue-mimicking phantom images and their values were subsequently plotted as a function of tissue-mimicking phantom thickness. For the synthetic and chicken phantoms, the DRS model included the optical absorption spectrum of nigrosin and oxy- and deoxyhemoglobin, respectively, measured using same spectrometer used for phantom measurements. The predicted slopes from DRS and IS were overlaid to compare the estimated depths against the true depths. A similar study was conducted using chicken tissue of varying thickness layered above a well of LS301.

2.9. Mouse models of breast cancer

All animal work was performed under an approved protocol by Washington University's Institutional Animal Care and Use Committee (IACUC). A mouse model of subcutaneous breast cancer was tested for fluorophore depth determination. Four Fox Chase SCID Beige mice (Charles River Laboratories, Wilmington, MA) were injected subcutaneously with 10^6 MDA-MB-468 S12 human breast tumor cells (ATCC) suspended in phosphate buffered saline into the right flank. The tumors grew approximately 1 cm in the longest dimension prior to tail vein injection with 60 μ M of LS301 (prepared in Achilefu Lab [29]) in human serum albumin (Sigma Aldrich, St. Louis, MO, USA) to test the effects of fluorophore concentration on depth retrieval accuracy. At 48 hours post LS301 injection, DRS measurements were acquired from the center of the intact tumor in vivo from mice #1-3 to extract optical properties for the y-intercept and slope for depth prediction as described above (DRS spectra and fits shown in Fig. S1). The optical properties for mouse 4 were estimated based on the average results from mice #1-3. The DRS model included optical absorption spectra of oxyhemoglobin, deoxyhemoglobin, and beta carotene. After DRS measurements and optical property extraction, DWEF imaging was performed to extract the ratiometric fluorescence for fluorophore depth determination. All in vivo imaging was conducted with mice under isoflurane anesthesia (2% vaporized in O_2).

After imaging, the mice were euthanized and the tumors were excised with the skin intact along the crease between the raised tumor boundary and healthy tissue to help demarcate the regions of the excised tumor that had been previously measured in vivo. The excised tumors were cut along the axial plane and then imaged in the custom-built DWEF imaging system to determine tumor margin thickness. Margin thickness of the excised tumor specimen was extracted for the region of tumor that was imaged using DWEF. The excised tumor fluorescence image collected at 780 nm excitation was first segmented to highlight the mouse tissue from background using an intensity threshold, and the tumor core was segmented from the non-cancerous tissue surrounding the tumor using adaptive thresholding from the Matlab function "imbinarize", a sensitivity of 0.15, and bright foreground polarity. The edges of tissue surface and tumor margin were extracted using Matlab's "edge" function with the Sobel edge detection method. Each edge was then fit with a spline and the distance between the inner and outer spline-fit edges was quantified by calculating the Euclidean distance between the intersection points of each curve and lines that

originated from the center of the tumor and spanned 0 to 90 degrees in order to cover the region imaged in vivo. The ex vivo extracted margin thickness was compared against the in vivo DWEF depth measurement from the same axial plane that the tumor was cut, as well as the 780 nm excited fluorescence signal to background ratio (SBR). The in vivo DWEF depth measurements were plotted against the ex vivo fluorescence depth measurements and the error between the DWEF and ex vivo cross section was calculated for each mouse. Furthermore, the in vivo DWEF depth measurements from all four mice were pooled together and compared against their ex vivo depth measurements. The pooled ex vivo extracted margin thicknesses from all mice were also compared to the corresponding 780 nm fluorescence SBR from the same axial locations. The data for pooled DWEF and SBR vs. ex vivo margin thickness were fit to a line forced through the origin and the slope of each line and Spearman correlation coefficient were extracted.

3. Results and discussion

3.1. Validation of depth determination in synthetic tissue-mimicking phantoms and chicken tissue

The custom-built dual wavelength excitation fluorescence imaging system provided high accuracy in determining the depth of an NIR fluorophore phantom beneath layers of synthetic tissue-mimicking phantoms and chicken breast tissue, as shown in Fig. 3.

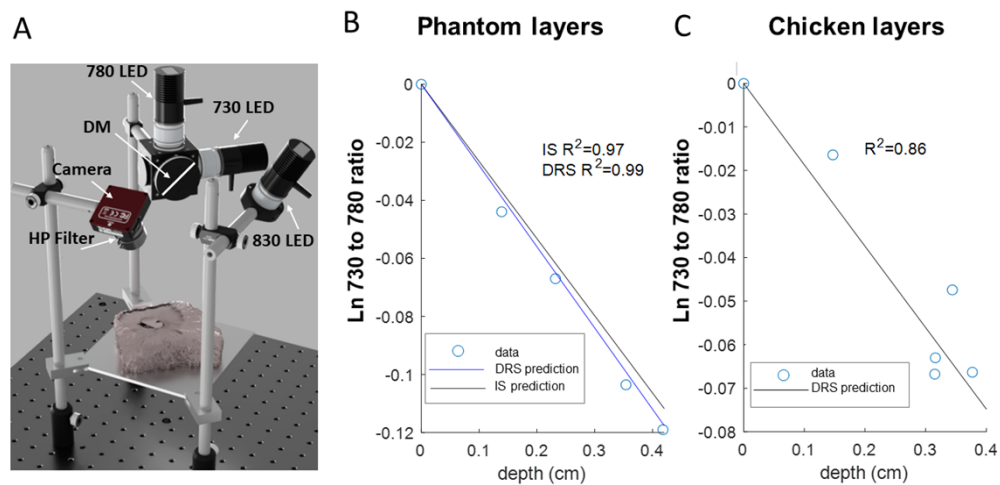


Fig. 3. Portable dual wavelength fluorescence imaging system determines NIR fluorophore depth under increasing thickness of tissue mimicking phantoms and chicken tissue. A) Schematic of experimental setup. Comparison between true depth of fluorophore beneath B) synthetic tissue mimicking phantom and C) chicken tissue. Ratiometric fluorescence imaging data plotted in blue circles, slope predicted from integrating sphere (IS) in black, and slope predicted using diffuse reflectance spectroscopy (DRS) in blue. Goodness of fit of the data to the DRS and IS predictions was measured using R^2 . (Abbreviations – DM–dichroic mirror, HP – high pass)

The ratiometric fluorescence intensity is depicted by blue circles and plotted with the corresponding synthetic tissue phantom thickness. A linear best fit line to the tissue-mimicking phantom data yielded a goodness of fit R^2 value 0.99, highlighting the linearity of the depth-dependent attenuation of light. In vivo, the depth of the fluorophore is unknown, and thus the look up table that relates a given ratio to a specific depth is created from the tissue optical properties. Optical properties were measured using an integrating sphere and diffuse reflectance spectroscopy as described in the methods, and the predicted line based on optical property

measurements is shown in black (integrating sphere) and blue (diffuse reflectance). The goodness of fit of the IS and DRS predictions are shown in Fig. 3(B), and yielded R^2 values of 0.97 and 0.99, respectively. The average error in depth prediction for the tissue mimicking phantoms was 164 μm with a standard deviation of 56 μm , which is likely a clinically acceptable amount of error. For example, when lumpectomy specimens are visualized using intraoperative CT, which has a spatial resolution of 100 μm , lesions that appear close to the specimen surface by a Radiologist's eye typically warrant removal of additional tissue termed a "shave margin" in the side of the tumor cavity where the lesion was found. However, the acceptable margin of error is application dependent and may be smaller for brain tumor resections, for example. In the chicken breast tissue experiment, the goodness of fit of the fluorescence ratio vs. depth to a linear curve was 0.89. The predicted slope based on DRS derived optical properties had a goodness of fit R^2 value of 0.86 and showed an average error of 0.47 mm with a standard deviation of 0.29 mm, which is minimal in a clinical environment. The prediction error was larger in the chicken breast tissue, which has many possible explanations. First, biological tissue is heterogeneous, and thus assigning a single set of optical property values for the chicken layers is not exact and expected to be an estimate. Second, measurement of the absolute chicken layer thicknesses was a challenge, and thus the gold standard measurement of the chicken layer thicknesses is not a perfect measure. Although we took steps to minimize this error, including creating chicken tissue holders to prevent the tissue from deforming during the experiment and measuring each layer thickness with calipers three distinct times and then taking the average, there was some variability between measurements which could help explain the higher error observed in chicken tissue. The reasonably low error even in heterogeneous tissues representative of what would be seen in an actual patient is promising for the clinical translation of the proposed technique.

3.2. *In vivo validation of depth determination in mouse tumor model injected with NIR tumor targeting fluorophore*

Dual wavelength excitation fluorescence imaging was performed in an *in vivo* mouse model of breast cancer, and the extracted clear margin thickness was compared to the clear margins measured from *ex vivo* fluorescence images from the excised tumors (Fig. 4).

DWEF yielded high accuracy in predicting tumor depth in a mouse model of breast cancer. Three image types from each mouse ($n=4$) are shown in Fig. 5, which include *in vivo* standard 780 nm excited fluorescence SBR (Column 1), *in vivo* DWEF (Column 2), and *ex vivo* fluorescent intensity images (Column 3) and tumor margin masks (Column 4) of each excised tumor sliced in half - which served as the gold standard margin thickness. The clear margin thickness based on DWEF (extracted at the dotted line in Column 2) and the excised tumor margins were plotted along the same line as the *ex vivo* tumor axial slicing (Column 5). Error between the gold standard cross section and DWEF (Column 6) was an average of 0.36 mm with a 0.23 mm standard deviation, demonstrating DWEF provided high accuracy. A likely contributor to the error observed in DWEF depth measurements is the fact that tissue naturally acts as a low pass spatial filter due to high light diffusion, thus changes on small spatial scales are blurred. In addition, although the authors worked diligently to orient and identify the exact *ex vivo* specimen locations mapped *in vivo*, there is the possibility for some experimental error due to the complexity of the methodology. Finally, the tumor segmentation method used did not always capture the knobby features of the tumor edge (see an example in Fig. S2), and this also contributed to error in the gold standard margin determination. This segmentation could be improved in future studies.

In addition, the DWEF and SBR results captured from the pixels that span the *ex vivo* axial slice location (shown via the dotted lines in Columns 1&2 in Fig. 5) from all four mice were pooled and plotted against the *ex vivo* gold standard margin thickness (Fig. 6). When performing a linear fit through the origin, a slope of 1.02 was achieved with DWEF, demonstrating DWEF's ability to quantify absolute depth. In contrast, a slope of 2.194 was achieved using fluorescence

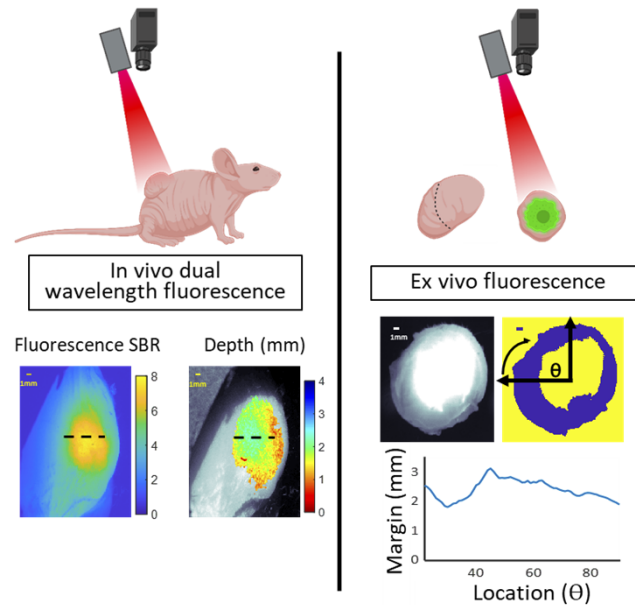


Fig. 4. Overview of in vivo and ex vivo tumor-targeted fluorophore imaging in tumor bearing mice. Fluorescence and dual wavelength excitation fluorescence images are first acquired in vivo (left panel) and intensity and depth maps are created. Mice are sacrificed and the tumor and surrounding tissue are excised. The tumor is cut down the transverse plane, and the tumor core is imaged to quantify the margin of tissue surrounding the fluorescently-tagged tumor (right panel). The location of the axial slice location is shown on the in vivo images with a dotted line.

SBR, providing little association with depth. Further, a Spearman correlation was calculated between margin thickness and DWEF and SBR results, yielding correlation coefficients of 0.68 and 0.22, respectively.

The fluorescence SBR is only a (weak) correlate to depth because the 3D fluorophore concentration is unknown, and the depth and concentration cannot be teased apart with a single wavelength when using a planar illumination geometry. The average error in the DWEF depth predictions was lower than the chicken breast tissue layering experiment, likely because the gold standard measurement (cutting the tumor in half with the skin intact and then performing fluorescence imaging to delineate tumor margin) was more exact. Similar to the chicken experiment, using point-based DRS to determine optical property values for each mouse does not capture tissue heterogeneity, and thus likely contributed to some of the observed error. However, the technique performed surprisingly well considering this over-simplification. The tradeoff between the simplicity of the DRS measurements and the accuracy of using this method to provide a global estimate of the optical properties should be weighed depending on the application and the degree of heterogeneity in the sample of interest. Taking this simplification a step further, mouse 4 provided an opportunity to explore the potential of using average tissue properties for a given tissue type. In relatively homogeneous tissues, prior capture of optical property information could be incorporated and provide an optical property confidence interval from which subsequent depth measurements could be determined, obviating the need for optical property capture for every tissue measured. This would further simplify the experimental setup and decrease imaging time.

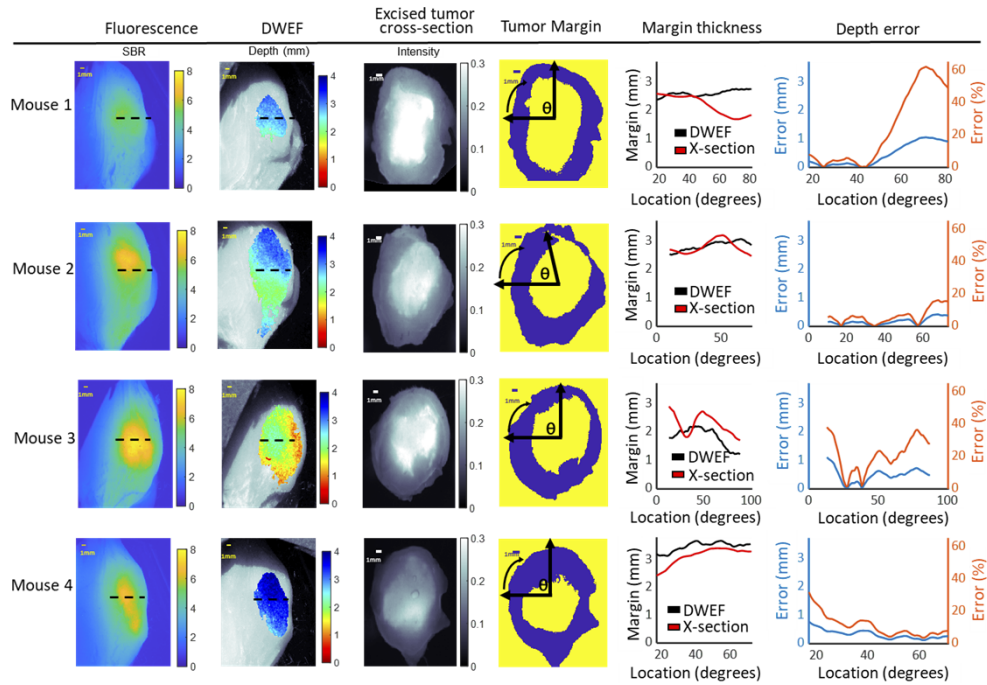


Fig. 5. In vivo dual wavelength excitation fluorescence (DWEF) imaging provides fluorophore depth with an average error of 340 μm . In vivo images from four tumor-bearing mice were generated using 780 nm excitation SBR (column 1) and DWEF (column 2). Excised tumors cut in the transverse plane were placed tumor core side down and imaged (column 3) to extract tumor margin (column 4). Comparison between in vivo DWEF and ex vivo margin thickness demonstrates in vivo fluorophore depth determination within 0.5-1 mm accuracy, and by extension, tumor margin determination within 0.5-1 mm accuracy. Error in depth determination between in vivo DWEF and ex vivo measurements are shown in mm (left y-axis) and percent error (right y-axis) (column 6).

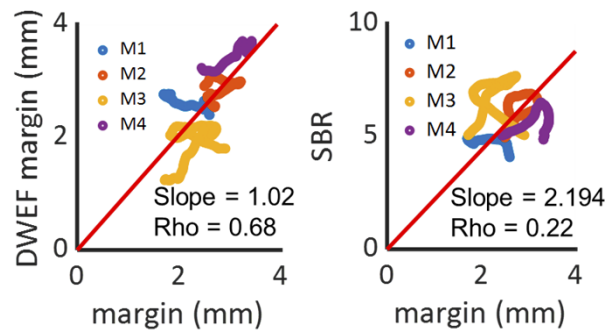


Fig. 6. In vivo dual wavelength excitation fluorescence (DWEF) has high accuracy in determining absolute margin thickness compared to fluorescent signal to background ratio (SBR) measurements. Left) Correlation between in vivo DWEF measurements from each mouse (M1-M4) and their corresponding gold standard tumor margin thickness. Right) Correlation between fluorescent SBR and gold standard tumor margin thickness.

3.3. Comparison to prior studies and implications for the field of FGS

Several groups have used ratiometric fluorescence imaging as a simple method to quantify fluorophore depth, including a recent study that demonstrated its utility in fluorescence-guided brain surgery [22]. However, our study is the first to apply the technique to NIR fluorophores, which have many advantages including increased penetration depth, reduced interference from autofluorescence, and consequently higher signal contrast compared to background. Due to these advantages, NIR fluorophores are being increasingly used in biomedical research and clinical studies. Indocyanine green is an FDA approved NIR fluorophore that is being used clinically for a wide array of applications, and numerous other NIR fluorophores are at different stages in the FDA approval process [1], including the tumor-targeting NIR fluorophore, LS301 [29], which was used in this study. Furthermore, the DWEF system described here is considerably simpler than previously reported methods. The DWEF system was purposely constructed using relatively low-cost components, including LEDs, an inexpensive CMOS camera, and low-cost spectrometer, to create a self-contained, portable imaging system that can be deployed in the operating room or pathology suite for rapid, intraoperative assessment of surgical margins. The system is enclosed to prevent the need for dimming or turning off the room lights, and DRS and DWEF measurements are completed within 5 minutes, minimizing impact on surgical/pathological workflow. At Washington University in St. Louis, where these studies were conducted, the standard of care for lumpectomy cases is to intraoperatively scan the excised breast specimens with CT followed by interpretation by a Radiologist to determine whether additional tissue should be removed from the tumor cavity. This process takes 5-10 minutes and our DWEF system could be substituted within this workflow. Although not completed at this time, we are in the process of developing a hardware and software pipeline to provide automated fluorophore depth maps within seconds. A major limitation of this study is the use of point-based DRS to provide optical property estimates for non-homogeneous tissue. This can be overcome by extracting 2D optical property maps using diffuse reflectance imaging or spatial frequency domain imaging which may be explored in future studies which would reduce time and minimize specimen handling. Additional limitations include difficulty handling non-flat surfaces due to the planar geometry. This can be resolved by acquiring 3D surface maps and performing more sophisticated tomographic reconstruction. However, for the current application, this added complexity is unnecessary as it is easy to compress the sample to a planar geometry for accurate data collection.

4. Conclusion

This study hypothesized that a simple dual wavelength excitation fluorescence imaging system could be designed, built, and tested for surgical margin determination. We successfully created this system and validated its performance in tissue-mimicking phantoms, chicken layering studies, and tumor margin determination studies with an *in vivo* mouse model of breast cancer. To our knowledge, this is the first implementation of such an approach in the near infrared where fluorescent contrast is improved due to low autofluorescent background and penetration depth is improved due to lower tissue scattering and reduced absorption of hemoglobin. The system showed high accuracy, with an average error of 164 μm , 0.44 mm, and 0.36 mm in tissue-mimicking phantoms, chicken layering studies, and *in vivo* mouse tumor margin determination, respectively. Furthermore, when compared head-to-head with fluorescence signal-to-background ratio, a commonly used metric to assess fluorophore location, the DWEF system showed superior accuracy and absolute correspondence to depth, whereas SBR showed poor accuracy and only a relative association to depth. Finally, the system presented is low-cost, rapid (<5 minutes for data capture), and portable. Further improvements to the optical property determination approach and automation of data capture and analysis will help expedite the path to clinical translation.

Funding. National Cancer Institute (R01 CA260855); National Institute of Biomedical Imaging and Bioengineering (R01 EB030987).

Acknowledgments. We would like to thank Mrs. Julie Prior of Washington University in St. Louis for assistance with experiments and support from the Optical Radiology Lab.

Disclosures. SA is a co-inventor on a US patent issued to Washington University covering LS301, which has been licensed to Integro Theranostics, which, however, did not support this work.

Data availability. Data underlying the results presented in this paper are not publicly available at this time but may be obtained from the authors upon reasonable request.

Supplemental document. See [Supplement 1](#) for supporting content.

References

1. S. B. Mondal, C. M. O'Brien, K. Bishop, R. C. Fields, J. A. Margenthaler, and S. Achilefu, "Repurposing molecular imaging and sensing for cancer image-guided surgery," *J. Nucl. Med.* **61**(8), 1113–1122 (2020).
2. R. R. Zhang, A. B. Schroeder, J. J. Grudzinski, E. L. Rosenthal, J. M. Warram, A. N. Pinchuk, K. W. Eliceiri, J. S. Kuo, and J. P. Weichert, "Beyond the margins: real-time detection of cancer using targeted fluorophores," *Nat. Rev. Clin. Oncol.* **14**(6), 347–364 (2017).
3. M. A. Stammes, S. L. Bugby, T. Porta, K. Pierzchalski, T. Devling, C. Otto, J. Dijkstra, A. L. Vahrmeijer, L.-F. de Geus-Oei, and J. S. D. Mieog, "Modalities for image-and molecular-guided cancer surgery," *Br. J. Surg.* **105**(2), e69–e83 (2018).
4. A. V. Dsouza, H. Lin, E. R. Henderson, K. S. Samkoe, and B. W. Pogue, "Review of fluorescence guided surgery systems: identification of key performance capabilities beyond indocyanine green imaging," *J. Biomed. Opt.* **21**(8), 080901 (2016).
5. I. Gage, S. J. Schnitt, A. J. Nixon, B. Silver, A. Recht, S. L. Troyan, T. Eberlein, S. M. Love, R. Gelman, J. R. Harris, and J. L. Connolly, "Pathologic margin involvement and the risk of recurrence in patients treated with breast-conserving therapy," *Cancer* **78**(9), 1921–1928 (1996).
6. K. C. Horst, M. C. Smitt, D. R. Goffinet, and R. W. Carlson, "Predictors of local recurrence after breast-conservation therapy," *Clin. Breast Cancer* **5**(6), 425–438 (2005).
7. M. Pilewskie and M. Morrow, "Margins in breast cancer: How much is enough?" *Cancer* **124**(7), 1335–1341 (2018).
8. H.-H. Lin, J.-K. Lin, C.-C. Lin, Y.-T. Lan, H.-S. Wang, S.-H. Yang, J.-K. Jiang, W.-S. Chen, T.-C. Lin, W.-Y. Liang, and S.-C. Chang, "Circumferential margin plays an independent impact on the outcome of rectal cancer patients receiving curative total mesorectal excision," *Am. J. Surg.* **206**(5), 771–777 (2013).
9. M. G. Bulbul, O. Tarabichi, R. K. Sethi, A. S. Parikh, and M. A. Varvares, "Does clearance of positive margins improve local control in oral cavity cancer? A meta-analysis," *Otolaryngol.–Head Neck Surg.* **161**(2), 235–244 (2019).
10. A. Funk, J. Heil, A. Harcos, C. Gomez, A. Stieber, H. Junkermann, A. Hennigs, G. Rauch, H. P. Sinn, F. Riedel, B. Schäfgen, S. Hug, A. Maier, M. Blumenstein, C. Domschke, S. Schott, M. Wallwiener, J. Rom, F. Schütz, C. Sohn, and M. Golatta, "Efficacy of intraoperative specimen radiography as margin assessment tool in breast conserving surgery," *Breast Cancer Res. Treat.* **179**(2), 425–433 (2020).
11. M. T. Garcia, B. S. Mota, N. Cardoso, A. L. C. Martimbianco, M. D. Ricci, F. M. Carvalho, R. Gonçalves, J. M. Soares Junior, and J. R. Filassi, "Accuracy of frozen section in intraoperative margin assessment for breast-conserving surgery: A systematic review and meta-analysis," *PLoS One* **16**(3), e0248768 (2021).
12. E. de Boer, N. J. Harlaar, A. Taruttis, W. B. Nagengast, E. L. Rosenthal, V. Ntziachristos, and G. M. van Dam, "Optical innovations in surgery," *Br. J. Surg.* **102**(2), e56–e72 (2015).
13. Q. Zhao, H. Jiang, Z. Cao, L. Yang, H. Mao, and M. Lipowska, "A handheld fluorescence molecular tomography system for intraoperative optical imaging of tumor margins," *Med. Phys.* **38**(11), 5873–5878 (2011).
14. L. Li, Y. Du, X. Chen, and J. Tian, "Fluorescence molecular imaging and tomography of matrix metalloproteinase-activatable near-infrared fluorescence probe and image-guided orthotopic glioma resection," *Molecular Imaging and Biology* **20**(6), 930–939 (2018).
15. M. N. v. Oosterom, P. Meershoek, M. M. Welling, F. Pinto, P. Matthies, H. Simon, T. Wendler, N. Navab, C. J. H. v. d. Velde, H. G. v. d. Poel, and F. W. B. v. Leeuwen, "Extending the hybrid surgical guidance concept with freehand fluorescence tomography," *IEEE Trans. Med. Imaging* **39**(1), 226–235 (2020).
16. O. Harbater, M. Ben-David, and I. Gannot, "Fluorescence lifetime and depth estimation of a tumor site for functional imaging purposes," *IEEE J. Sel. Top. Quantum Electron.* **16**(4), 981–988 (2010).
17. J. T. Smith, E. Agounoun, S. Gioux, and X. Intes, "Macroscopic fluorescence lifetime topography enhanced via spatial frequency domain imaging," *Opt. Lett.* **45**(15), 4232–4235 (2020).
18. Y. Chen, W. Xie, A. K. Glaser, N. P. Reder, C. Mao, S. M. Dintzis, J. C. Vaughan, and J. T. C. Liu, "Rapid pathology of lumpectomy margins with open-top light-sheet (OTLS) microscopy," *Biomed. Opt. Express* **10**(3), 1257–1272 (2019).
19. A. K. Glaser, N. P. Reder, Y. Chen, E. F. McCarty, C. Yin, L. Wei, Y. Wang, L. D. True, and J. T. C. Liu, "Light-sheet microscopy for slide-free non-destructive pathology of large clinical specimens," *Nat. Biomed. Eng.* **1**(7), 0084 (2017).

20. G. Brandon, T. I. Collin, L. Yi, C. Yu, and H. Huang-Chiao, "Depth-resolved imaging of photosensitizer in the rodent brain using fluorescence laminar optical tomography," *J. Biomed. Opt.* **25**, 1–14 (2020).
21. J. P. Miller, D. Maji, J. Lam, B. J. Tromberg, and S. Achilefu, "Noninvasive depth estimation using tissue optical properties and a dual-wavelength fluorescent molecular probe in vivo," *Biomed. Opt. Express* **8**(6), 3095–3109 (2017).
22. D. J. Wirth, M. Sibai, B. C. Wilson, D. W. Roberts, and K. Paulsen, "First experience with spatial frequency domain imaging and red-light excitation of protoporphyrin IX fluorescence during tumor resection," *Biomed. Opt. Express* **11**(8), 4306–4315 (2020).
23. K. K. Kolste, S. C. Kanick, P. A. Valdes, M. Jermyn, B. C. Wilson, D. W. Roberts, K. D. Paulsen, and F. Leblond, "Macroscopic optical imaging technique for wide-field estimation of fluorescence depth in optically turbid media for application in brain tumor surgical guidance," *J. Biomed. Opt.* **20**(2), 026002 (2015).
24. A. V. Khilov, M. Y. Kirillin, D. A. Loginova, and I. V. Turchin, "Estimation of chlorin-based photosensitizer penetration depth prior to photodynamic therapy procedure with dual-wavelength fluorescence imaging," *Laser Phys. Lett.* **15**(12), 126202 (2018).
25. J. Michael, K. K. Kolbein, P. Julien, S. Guillaume, M. A.-R. Leticia, D. P. Keith, W. R. M. D. David, C. W. Brian, P. Kevin, and L. Frederic, "Macroscopic-imaging technique for subsurface quantification of near-infrared markers during surgery," *J. Biomed. Opt.* **20**, 1–9 (2015).
26. G. Hong, A. L. Antaris, and H. Dai, "Near-infrared fluorophores for biomedical imaging," *Nat. Biomed. Eng.* **1**(1), 0010 (2017).
27. J. Jiao, J. Zhang, F. Yang, W. Song, D. Han, W. Wen, and W. Qin, "Quicker, deeper and stronger imaging: A review of tumor-targeted, near-infrared fluorescent dyes for fluorescence guided surgery in the preclinical and clinical stages," *Eur. J. Pharm. Biopharm.* **152**, 123–143 (2020).
28. A. Haque, M. S. H. Faizi, J. A. Rather, and M. S. Khan, "Next generation NIR fluorophores for tumor imaging and fluorescence-guided surgery: A review," *Bioorg. Med. Chem.* **25**(7), 2017–2034 (2017).
29. D. Shen, B. Xu, K. Liang, R. Tang, G. P. Sudlow, C. Egbulefu, K. Guo, A. Som, R. Gilson, D. Maji, S. Mondal, L. Habimana-Griffin, W. J. Akers, S. Li, Y. Liu, S. Bloch, S. Kurkure, Z. Nussinov, A. Seidel, S.-W. D. Tsen, and S. Achilefu, "Selective imaging of solid tumours via the calcium-dependent high-affinity binding of a cyclic octapeptide to phosphorylated Annexin A2," *Nat. Biomed. Eng.* **4**(3), 298–313 (2020).
30. S. L. Jacques, "Optical properties of biological tissues: a review," *Phys. Med. Biol.* **58**(11), R37–R61 (2013).
31. J. Swartling, J. Svensson, D. Bengtsson, K. Terike, and S. Andersson-Engels, "Fluorescence spectra provide information on the depth of fluorescent lesions in tissue," *Appl. Opt.* **44**(10), 1934–1941 (2005).
32. T. J. Farrell, M. S. Patterson, and B. Wilson, "A diffusion theory model of spatially resolved, steady-state diffuse reflectance for the noninvasive determination of tissue optical properties in vivo," *Med. Phys.* **19**(4), 879–888 (1992).
33. A. J. Welch and M. J. C. Van Gemert, *Optical-thermal Response of Laser-irradiated Tissue* (Springer, 2011), Vol. 2.
34. S. Jacques, "Library," retrieved <https://omlc.org/~jacquess/library.html>.
35. S. Prah, "Everything I think you should know about Inverse Adding-Doubling," Oregon Medical Laser Center, St. Vincent Hospital **1**, 1–74 (2011).
36. P. Krauter, S. Nothelfer, N. Bodenschatz, E. Simon, S. Stocker, F. Foschum, and A. Kienle, "Optical phantoms with adjustable subdiffusive scattering parameters," *J. Biomed. Opt.* **20**(10), 105008 (2015).
37. V. V. Tuchin, *Tissue Optics: Light Scattering Methods and Instruments for Medical Diagnosis, Second Edition*, 2nd ed. (SPIE Press, Bellingham, 2007).
38. A. J. Ruiz, M. Wu, E. P. M. LaRochelle, D. Gorpas, V. Ntziachristos, T. J. Pfefer, and B. W. Pogue, "Indocyanine green matching phantom for fluorescence-guided surgery imaging system characterization and performance assessment," *J. Biomed. Opt.* **25**(05), 1–15 (2020).
39. D. Gorpas, M. Koch, M. Anastasopoulou, U. Klemm, and V. Ntziachristos, "Benchmarking of fluorescence cameras through the use of a composite phantom," *J. Biomed. Opt.* **22**(1), 016009 (2017).